PAPER

Formation of capillary structures with highly viscous fluids in plane microchannels

Samira Darvishi and Thomas Cubaud*

A detailed experimental study of capillary structures made with high-viscosity fluids is conducted in plane microchannels. We examine the possibility to emulsify fluids *via* viscous folding instabilities using continuous microflows. Non-wetting capillary threads are formed in a sheath of immiscible liquids for a wide range of viscosity and flow rate ratios using symmetric hydrodynamic focusing sections. Downstream, threads are significantly deformed in a diverging channel connected to a long plane microchannel. Adjusting the residence time of thread structures in the plane channel allows us to produce various degrees of fold coalescence. Three typical regimes are identified: thread breakup, partial fold coalescence, and complete fold coalescence. The geometrical features of evolving folds are measured and related to material properties, flow parameters, and microgeometries. This study shows that folded structures offer the opportunity to examine novel interfacial configurations and provides a set of microfluidic techniques for improved manipulation of viscous materials with thin immiscible lubricants at the small scale.

1. Introduction

The behavior of viscous multiphase flows at the small scale is of great technological importance in fields as diverse as enhanced oil recovery,[1] biodiesel production,[2] and crude oil processing.[3] Thick materials, such as glycerol, oils, concentrated emulsions, or mucus, are common in nature and industrial processes. In general, the flow of viscous fluids is characterized by a high resistance to shear and, as a result, thick materials can readily remain attached to surfaces. This basic property can be either detrimental – for instance during oil transport in pipelines with the buildup of wax on walls[4] – or advantageous, such as during the locomotion of gastropods[5] or in the digestive system[6] where mucus provides lubrication. In the respiratory system, however, the excess of high-viscosity sputum can cause obstruction of airways and lead to severe diseases, such as cystic fibrosis.[7]

An important flow phenomenon, which occurs between liquids having disparate viscosities in compact ducts, consists in the possibility for streams to reorganize and form a central viscous core, *i.e.*, a viscous thread, surrounded by an annulus made of less viscous constituents near the solid walls. The self-lubrication property of thick multiphase flows overall reduces viscous dissipation[8] and has been observed for a variety of length-scales, including during the flow of molten rocks in volcanic conduits,[9] oil transport in pipelines,[10] as well as the microflow of viscoelastic fluids.[11]

Microfluidic devices offer the opportunity to finely control flow geometries and enable advanced fluid manipulations at the small scale. In addition to facilitating the production of individual bubbles and droplets,[12–17] simple microfluidic methods can be implemented to produce viscous threads.[18–20] Jets and threads have been extensively studied in unbounded systems, *i.e.*, in the context of free-boundary flows.[21] In particular, a variety of hydrodynamic destabilization processes, including Rayleigh–Plateau[22,23] (*i.e.*, segmentation of fluid filaments into droplets due to capillary force), coalescence[24,25] (*i.e.*, fusion between droplets), and viscous buckling[26–31] (*i.e.*, folding and coiling of viscous "ropes" impinging on surfaces) instabilities, yield complex responses of fluid interfaces. In confined systems, fluid interactions with solid boundaries can lead to Saffman–Taylor instabilities[32,33] (*i.e.*, formation of fingers during the displacement of a low-viscosity fluid into a stagnant high-viscosity phase) and a range of wetting dynamics.[34–38] In general, the non-uniqueness of free-boundary flow configurations and the variety of non-linear phenomena involved represent a significant theoretical challenge. In practice, however, simple microfluidic geometries allow for systematically exploring novel flow arrangements, and the laminar properties of creeping flows permit a deterministic approach to pattern formation with high-viscosity fluids. Overall, a better understanding of confined free-boundary flows with highly viscous fluids is important for characterizing the lubricated transport and rheological behavior of soft materials with solvents in microsystems.

Here, we examine the behavior of viscous threads flowing within a sheath of immiscible fluids using a microfluidic chamber having a constant gap thickness. We show that microfluidic

Department of Mechanical Engineering, Stony Brook University, Stony Brook, NY, 11794 USA. E-mail: thomas.cubaud@stonybrook.edu

confinement essentially restricts thread deformations to a planar field of view and permits the formation of elaborate continuous capillary structures. The fluid pairs used in experiments primarily consist of silicone oils and isopropanol. The oil–alcohol fluid pair is particularly relevant for energy applications and allows us to access the relatively uncharted regions of microfluidic flow regimes at large capillary numbers.

We first discuss the experimental setup, fluid properties, and channel design. Lubricated threads of viscous oils are formed using a symmetric hydrodynamic focusing section with channels that are square in cross-section. Downstream, the chamber consists of a diverging channel followed by a planar section of constant width connected to a converging section. As threads enter the diverging channel, they experience a viscous folding instability, which significantly distorts slender viscous structures. In compact microchannels, we previously showed that interfacial forces tend to stabilize threads through a capillary unfolding process for low capillary numbers.[39] In plane geometries, however, the effect of interfacial tension on folds is non-trivial since threads are relatively free to deform normal to the flow direction. In the current study of capillary thread behavior in plane microchannels, we show that bended fluid structures naturally evolve due to the action of viscous and capillary forces, and the degree of coalescence between adjacent folds is tunable with flow rates of injection and fluid properties. A general phase diagram of flow patterns is presented, including thread breakup, partially coalesced folds, and fully coalesced folds.

A detailed study of the evolving shape of folded micro-threads is then conducted in relation with flow capillary numbers and fluid viscosity contrasts. We monitor the amplitude and wavelength of capillary structures along the flow direction and provide the corresponding scaling laws based on viscosity contrasts and capillary numbers. Relating measurements of thread velocity, envelope amplitude, and input flow parameters with a mass conservation argument is used to estimate the evolution of the film thickness between the lubricated capillary structures and top and bottom walls of the chamber. Finally, we document flow regimes where threads can be utilized to either emulsify the highly viscous oil into the low-viscosity phase or "reverse" emulsify small amounts of alcohol into thick oils. This work shows that folded structures offer the opportunity to examine novel interfacial configurations and provides a set of microfluidic techniques for improved manipulation of very viscous fluids at the small scale.

2. Materials and methods

The microfluidic module is constructed using standard silicon-based microfabrication techniques.[40] A double-side-polished silicon wafer of thickness $h = 250$ μm is etched-through using deep reactive ion etching and then sealed between two borosilicate glass plates using anodic bonding.[41] Such hard microfluidic modules are non-deformable and allow for handling high-viscosity fluids at the small scale. The channel geometry consists of three consecutive elements: (1) a hydrodynamic focusing section connected to a square inlet microchannel to form steady threads; (2) a long microfluidic chamber of total length $L = 27h$, which starts with a diverging section of length $L_D = 3.5h$ and an aperture angle of $\pi/2$, followed by a plane channel of constant

width $w = 8h$ and length $L_P = 20h$, and ends with a converging section of length $L_C = 3.5h$; and (3) an outlet square channel [Fig. 1(a)]. Aside from the initial focusing section, the channel geometry has a mirror symmetry with respect to the flow direction, and the large aspect ratio of the plane channel, $w/h = 8$, allows for comparing flow behaviors with two-dimensional approximations. Given the aperture angle of the diverging channel, the point located at $-h/2$ from the transition between the inlet and the diverging channel is labeled as a "virtual source" and corresponds to $x = 0$. In a similar fashion, the point located at $h/2$ from the transition between the converging channel and the outlet channel is labeled as a "virtual sink". Source and sink refer to elementary two-dimensional flow patterns, which flow radially outward and inward respectively. Such approximations are useful for describing creeping flows in slit diverging and converging microchannels.[42] Here, the effective microchamber length between virtual source and sink is $28h$.

High-viscosity threads are formed in the focusing section with the continuous introduction of silicone oil (L1) of viscosity η_1 into the central channel at the volumetric flow rate Q_1, and the symmetric injection of isopropanol alcohol (L2) of viscosity η_2 in the side-channels at a total flow rate Q_2 using high-pressure syringe pumps (New Era Pump Systems, Inc.). In the asymptotic regime associated with large dynamic viscosity ratios $\chi = \eta_1/\eta_2 > 15$, previous studies[19,20,43] showed that this fluid injection scheme yields the formation of a core-annular flow in the square inlet channel where the more viscous liquid (L1) forms a thread lubricated by the less viscous sheath liquid (L2). The resulting initial thread diameter ε_0 solely depends on the flow rate ratio $\varphi = Q_1/Q_2$ according to $\varepsilon_0/h = (\varphi/2)^{1/2}$. Therefore, the initial size of the filament upstream from the microfluidic chamber is independent of the viscosity contrast χ. This property is utilized to produce a variety of threads in the inlet channel and probe the influence of χ on their deformations in the chamber. Four silicone oils (L1) (Gelest) having kinematic viscosities $\nu_1 = 200$, 500, 1000 and 5000 cSt – with corresponding dynamic viscosities $\eta_1 = 193$, 486, 971, and 4865 cP – are tested with isopropanol (L2) (Sigma-Aldrich) having a dynamic viscosity $\eta_2 = 2.24$ cP. Overall, the dynamic viscosity contrast χ ranges between 86 and
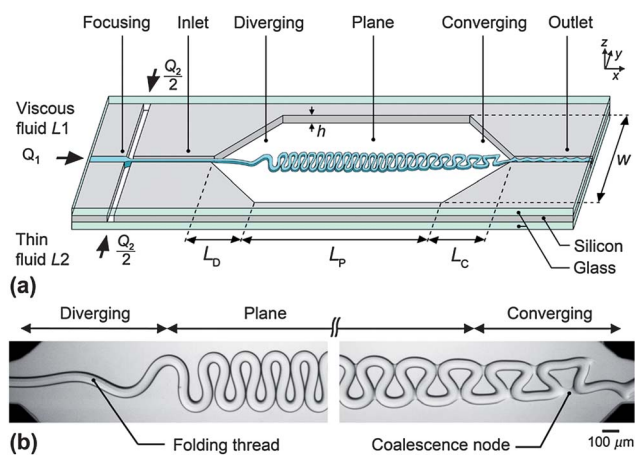
Fig. 1 (a) Schematic of the microchannel layout. (b) Experimental micrographs of a folding thread in the diverging and converging sections, flow rates $Q_1 = 50$ and $Q_2 = 600$ μL min⁻¹, viscosity contrast $\chi = 2172$.

2172. The interfacial tension γ_{12} is measured using the combined capillary rise technique[44] and ranges between 2.4 and 2.7 mN m^{-1}. Fluid pairs are selected to examine the deformation of non-wetting capillary threads (i.e., contact angle $\theta \approx 180°$).

To investigate the influence of flow history on thread deformations, microflow patterns are observed at different locations in the network with a high-speed camera (HG-100K, Redlake). The flow module is placed on top of an inverted microscope equipped with a moving stage (Accu-Scope), and illumination is provided with a high-intensity halogen light (Dolan-Jenner) set about 10 cm above the chip. For a given set of fluid pair ($L1$ and $L2$) and injection flow rates (Q_1 and Q_2), characteristic fields of view correspond to: (1) the inlet channel with the diverging section and the first half of the plane chamber and (2) the second half of the chamber with converging and outlet channels. Depending on location and flow properties, different types of deformations are observed. Here, we turn our attention to deformations associated with relatively small threads (i.e., in the threading regime).[42] Threads of $L1$ are lubricated in a sheath flow of $L2$ (i.e., lubricant), the streamlines of which are controlled by solid micro-geometries. In the diverging channel, a thread experiences a typical viscous folding instability due to flow deceleration that produces an axial compressive stress along the filament [Fig. 1(b)]. The viscous folding instability alters the viscous thread morphology and leads to the formation of a periodic structure having an envelope amplitude A and a spatial period λ. This capillary structure evolves in the plane channel depending on fluid properties and flow parameters. In particular, nearby folds can partially or fully merge due to the coalescence of various thread segments, which are in close contact. Given the large viscosity of $L1$, this dynamical process is relatively slow compared with the convection time-scale of $L2$, and the fold coalescence phenomenon can be adjusted with fluid rates of the injection in the chamber.

3. Results and discussions

3.1 Phase-diagram

The morphology of distorted threads in the chamber primarily depends on the initial thread size ε_0 and the injection capillary number Ca_0. While the thread size is a function of the flow rate ratio, $\varepsilon_0/h = [Q_1/(2Q_2)]^{1/2}$, the injection capillary number is based on the absolute values of flow rates according to $Ca_0 = \eta_1 J_0/\gamma_{12}$, where $J_0 = (Q_1 + Q_2)/h^2$ is the multiphase superficial velocity in the inlet square channel. The capillary number, which compares viscous to capillary stresses, is particularly important here because the viscous buckling instability tends to increase the fluid interfacial area while surface tension forces act to reduce it. Hence, confined folded capillary structures strongly depend on Ca_0.

To classify flow regimes, we examine patterns at the end of the plane channel to allow enough time for bended filaments to age under the influence of viscous and capillary forces. For χ varying between 86 and 2172, three distinct regimes are identified: (a) breakup of thin threads at large Ca_0, (b) partial fold coalescence of thick threads at large Ca_0, and (c) complete fold coalescence at low Ca_0 [Fig. 2]. Besides subtle differences at the transition
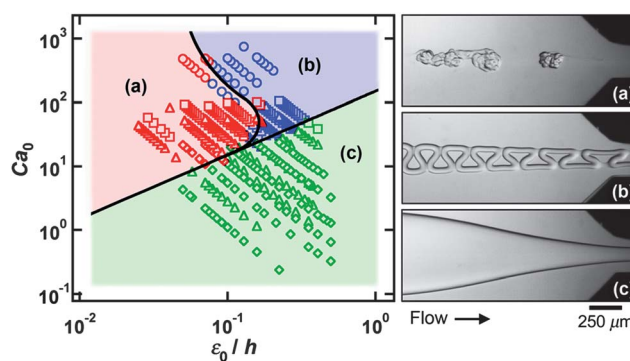
Fig. 2 Phase-diagram of typical flow patterns observed in the converging section with initial capillary number Ca_0 vs. normalized initial thread size ε_0/h, viscosity contrast $\chi = 86$ ($\diamond$), 217 ($\triangle$), 433 ($\square$), and 2172 ($\bigcirc$), with experimental micrographs, flow rates in µL min^{-1}: (a) Breakup regime $Q_1 = 5$, $Q_2 = 650$, and $\chi = 217$. (b) Partial fold coalescence regime $Q_1 = 20$, $Q_2 = 400$, and $\chi = 2172$. (c) Complete fold coalescence regime, $Q_1 = 50$, $Q_2 = 400$, and $\chi = 86$.

between flow patterns, experimental findings show that each regime is located in a well-defined region of our parameter space.

The breakup regime corresponds to the segmentation of thin threads into irregular viscous chunks (i.e., high-viscosity droplets) [Fig. 2(a)]. Near the convergence, the Rayleigh–Plateau instability can induce wide variations of the envelope amplitude of folded threads that are indicative of the breakup regime. In general, the distance between folds λ decreases along the first part of the microchamber. As a result, adjacent folds make direct contact with one another and coalesce. Although the complete coalescence of two millimetric water droplets in air is relatively fast ($\sim$1 ms),[45] fold coalescence in our system is relatively slow due to the high viscosity of folds made of $L1$ and the presence of the viscous environment (i.e., liquid $L2$). The regime associated with partial coalescence is identified when folded structures are still optically discernible near the end of the chamber [Fig. 2(b)]. For a given fluid pair, low capillary numbers Ca_0 are obtained for small flow velocity, i.e., for long thread residence time in the chamber. In this case, folds fully coalesce and form a uniform high-viscosity stream [Fig. 2(c)].

Although the transition curve between breakup and partial coalescence is rather complex, experimental results suggest that the transition between the full coalescence regime and the other two regimes is delineated by the expression $Ca_{0,c} \approx 150(\varepsilon_0/h)$ [Fig. 2]. The capillary number can be expressed as $Ca_0 = \tau^*/\tau_R$, where τ_R is the residence time of threads in the chamber, $\tau_R = L/J_w$, with the multiphase flow velocity in the chamber being $J_w \approx (Q_1 + Q_2)/(hw)$, and τ^* is a capillary time-scale based on fluid properties and chamber geometry with $\tau^* = \eta_1 Lw/(\gamma_{12}h)$. The transition line between the full coalescence regime and the other two regimes is used to express the critical residence time for full fold coalescence in the chamber such as $\tau_{R,c} \approx a\eta_1 Lw/(\gamma_{12}\varepsilon_0)$ with the geometrical constant $a = 1.44$. Therefore, for long residence times, $\tau_R > \tau_{R,c}$, structures are seen to be fully coalesced when leaving the chamber. For short residence times, $\tau_R < \tau_{R,c}$, small threads rupture into droplets and large threads form partially coalesced structures. An intriguing property of this system is that the fold coalescence time-scale $\tau_{R,c}$ (i.e., the critical residence time for coalescence) is inversely proportional to the thread size ε_0. In

the following sections, we show that this effect is due to the interplay of viscous and capillary instabilities combined with self-lubrication phenomena in constrained microgeometries.

3.2 Initial thread morphology

3.2.1 Envelope amplitude. To better understand the influence of viscous and capillary forces on thread dynamics, we first turn our attention to the initial evolution of viscous filaments in the chamber. Threads are initially straight in the square channel and fold as they enter the diverging section. Although the overall thread response to a change in geometrical flow confinement follows that of the channel, in previous work,[39] we showed that the shape of miscible fluid folds strongly depends on the viscosity contrast χ and initial thread size ε_0. Here, to focus on the effect of capillary forces, we fix material properties and examine the dynamics of threads having similar initial thread size ε_0, i.e., for $\chi = 217$ and $\varphi = 0.1$ [Fig. 3]. Setting a constant flow rate ratio φ while changing the absolute values of the flow rates Q_1 and Q_2 reduces the number of varying parameters to the sole capillary number Ca_0.
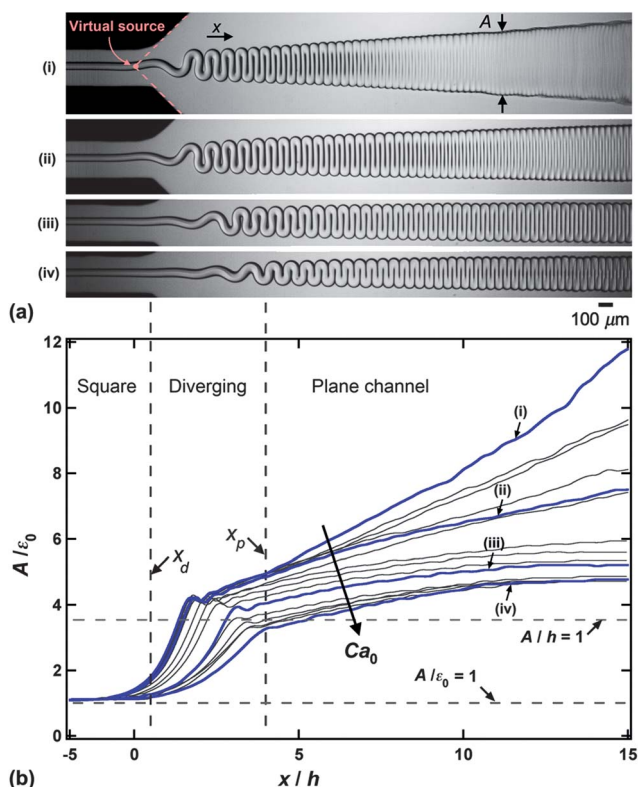
Fig. 3 Influence of the injection capillary number Ca_0 on the spatial evolution of the envelope amplitude A for constant flow rate ratio $\varphi = 0.1$ and viscosity contrast $\chi = 217$. (a) Experimental micrographs, flow rates in $\mu L \min^{-1}$: (i) $Ca_0 = 3$, $Q_1 = 5$, and $Q_2 = 50$; (ii) $Ca_0 = 6$, $Q_1 = 10$, and $Q_2 = 100$; (iii) $Ca_0 = 30$, $Q_1 = 50$, and $Q_2 = 500$; and (iv) $Ca_0 = 60$, $Q_1 = 100$, and $Q_2 = 1000$. (b) Evolution of the normalized envelope amplitude A/ε_0 as a function of the scaled distance along the chamber x/h. The position x_d indicates the transition between the square and the diverging channel, and the coordinate x_p locates the transition between the diverging and the plane channels. Thick lines correspond to the flow regimes displayed in (a).

In steady flows, threads fold within an envelope, the width of which, $A(x)$, depends on the location in the chamber. For a given set of flow rates, the spatial evolution of the envelope is extracted from experiments by superimposing consecutive images from a high-speed movie onto a composite image. The width of the envelope A is then computed from this image and x is set to 0 at the virtual source in the square channel, which is located at $-h/2$ from the transition between the square and the diverging channel.

Fig. 3(b) shows the spatial evolution of the envelope amplitude normalized by the initial thread size A/ε_0 as a function of the dimensionless position x/h when Ca_0 increases from 3 to 60. Data show that the spatial growth of A diminishes with the injection capillary number Ca_0. This result is relatively counter-intuitive since more interfacial fluid area is initially produced at low capillary numbers Ca_0. However, a close inspection of the flows associated with low Ca_0 reveals that folds coalesce near the middle of the plane channel [Fig. 3(a)-(i) for $x/h \sim 15$]. This phenomenon reduces the $L1/L2$ interfacial area of capillary threads over the entire chamber. In addition, similar to the flow of bubbles and droplets in compact ducts,[46–48] thinner film thicknesses δ are expected between the structures made of $L1$ and the top and bottom walls of the chamber in the low Ca_0 situation. Based on a mass conservation argument, we conjecture that to compensate for the relatively high shear stress present in the thin film of $L2$ for low Ca_0 flows, the envelope amplitude A increases along the plane channel to reduce the local velocity of $L1$. Consequently, the flow deceleration in the plane channel produces a larger compressive stress on threads in the diverging channel and the viscous folding instability appears more pronounced for low Ca_0 (Fig. 3(a)). As a result, we conclude that viscous and capillary forces initially act together and cause an increase of the thread area in the diverging channel.

The spatial evolution of the amplitude $A(x)$ exhibits two distinct regimes: a quadratic increase in the opening of the diverging channel ($A \sim x^2$) followed by a nearly linear growth in the beginning of the plane section ($A \sim x$). The transition between these two regimes is characterized by a local maximum in the amplitude [Fig. 4(a)].

Since the initial filament diameter ε_0 plays a critical role in thread dynamics, we confirm that, upstream in the square channel ($x/h \approx -5$), the optically measured thread sizes ε_m are in good agreement with theory, i.e., $\varepsilon_0/h = (\varphi/2)^{1/2}$, for the dataset characterized by $\varphi = 0.1$, $\chi = 217$, and Ca_0 varying between 3 and 60 [Fig. 4(b) – top]. For significant thread deceleration in the chamber (i.e., for low Ca_0), threads display undulations in the square inlet channel near the divergence. To quantify this effect, we measure the envelope amplitude A_d at the transition between these channels, i.e., at $x = x_d$. Fitting data with a simple power function suggests that A_d decreases with the capillary number Ca_0 according to $A_d/\varepsilon_0 \approx 1 + 1.53 Ca_0^{-1/2}$ [Fig. 4(b) – bottom]. The fact that A_d/ε_0 is larger than unity demonstrates that the viscous folding instability occurs as early as in the square inlet microchannel. Using the numerical value of A_d, we fit the thread envelope amplitude $A(x)$ in the divergence before it reaches the local maximum with $A/\varepsilon_0 = A_d/\varepsilon_0 + k_1(x/h)^2$, where the coefficient k_1 also depends on Ca_0 according to $k_1 \approx 2.1 Ca_0^{-1/2}$ [Fig. 4(c)].

Next, we quantify the amplitude growth at the start of the plane channel for x/h varying between 4 and 10. For $Ca_0 < 15$,
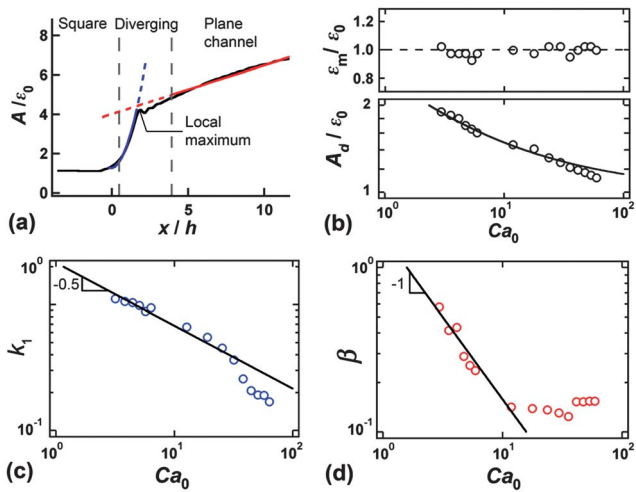
Fig. 4 Detailed evolution of normalized envelope amplitude A/ε_0 for fixed flow rate ratio $\varphi = 0.1$ and $\chi = 217$. (a) Schematic of spatial evolution of the amplitude fit with a quadratic function at the beginning of the diverging section, $A/\varepsilon_0 = A_d/\varepsilon_0 + k_1(x/h)^2$ (blue line), and fit with a linear function at the beginning of the plane channel, $A/\varepsilon_0 = A_p/\varepsilon_0 + \beta(x/h)$ (red line). (b) Top: measured initial thread size in the square channel normalized by the calculated thread size, $\varepsilon_m/\varepsilon_0$ as a function of Ca_0, dashed line: $\varepsilon_m/\varepsilon_0 = 1$. Bottom: normalized envelope amplitude at the beginning of the divergence A_d/ε_0 (at x_d) vs. Ca_0, solid line: $A_d/\varepsilon_0 = 1 + 1.53Ca_0^{0.5}$. (c) Evolution of the coefficient k_1 with Ca_0, solid line: $k_1 = 2.1Ca_0^{-0.5}$. (d) Coefficient β as a function of Ca_0, solid line: $\beta = 1.6Ca_0^{-1}$.

the amplitude is reasonably well fit with $A/h = A_p/h + \beta(x/h)$, where A_p is the envelope amplitude at $x = x_p$ and $\beta \approx 1.6Ca_0^{-1}$. For larger values of Ca_0, the coefficient β is very small and appears to saturate. The cut-off value for the capillary number ($Ca_0 = 15$) corresponds to the transition between the complete coalescence and the partial coalescence regimes for $\varphi = 0.1$. For the complete coalescence regime ($Ca_0 < 15$), the envelope amplitude of the folded thread A linearly increases with distance and reaches a maximum near the transition between the plane and the converging channels ($x/h \sim 24$). By contrast, for the partial coalescence regime ($Ca_0 > 15$), the envelope amplitude reaches a maximum near the middle of the plane section ($x/h \sim 14$).

The partial coalescence regime offers the opportunity to measure a single value of the envelope width A in the central region of the chamber for a variety of flow rates and viscosity contrasts. In compact microchannels of width w, previous work[39] conducted with miscible fluid threads showed that the amplitude of uniformly folded threads scales as $A/w \approx k\varphi^{1/2}$, where $k = c\chi^{1/4}$ and c is a geometrical constant. A comparable trend is found in the current study and the corresponding envelope amplitude A is fit with

$$A/w \approx c\chi^{1/4}\varphi^{1/2}, \qquad (1)$$

where $c \approx 0.085$ [Fig. 5(a)]. We interpret the constant c to be a geometrical prefactor on the order of the channel aspect ratio $h/w = 1/8$. Overall, eqn (1) is in good agreement with the theory of periodic folding of viscous sheets in air where the amplitude of folding scales as $A \sim \eta^{1/4}$, with η being the viscosity of the liquid sheet.[49,50] In our microfluidic scenario, which involves steady injections of two liquids and the absence of impinging surfaces,
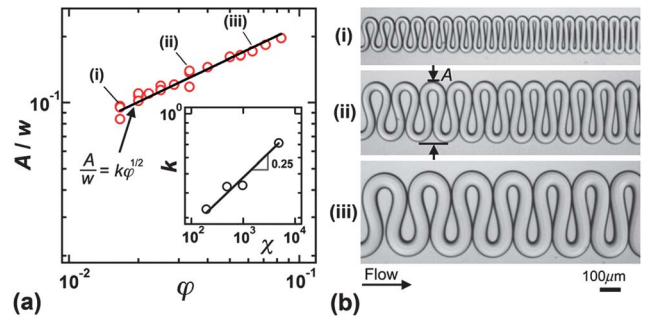

Fig. 5 (a) Envelope amplitude A/w vs. flow rate ratio φ, viscosity contrast $\chi = 2172$, solid line: $A/w = k\varphi^{1/2}$. Inset: Prefactor k as a function of viscosity contrast χ, solid line: $k = 0.085\chi^{1/4}$. (b) Experimental micrographs, flow rates in µL min^{-1}: (i) $Q_1 = 5$ and $Q_2 = 400$, (ii) $Q_1 = 20$ and $Q_2 = 600$, and (iii) $Q_1 = 50$ and $Q_2 = 600$.

the viscosity contrast χ is equivalent to the absolute viscosity η of liquid sheets in air.

As the viscosity contrast χ increases from 86 to 2172, the envelope amplitude of folded threads remains more constant along the microfluidic chamber. For instance, Fig. 5(b) shows that the shape of highly viscous threads ($\chi = 2172$) does not significantly vary in the central region of the chamber. The fold wavelength, however, is seen to noticeably decrease along the flow direction.

3.2.2 Fold wavelength. The periodic folding of capillary threads produces complex flow structures that are characterized by an evolving spatial period λ along the microfluidic network. To investigate the spatial development of λ, we track specific folds using fast imaging and record the wavelength as a function of position. In the diverging section, folds are growing and present asymmetrical features. To circumvent this limitation, the distance between two consecutive crests located at x_1 and x_2 is used to estimate the wavelength $\lambda = |x_2 - x_1|$ at position $x = (x_2 + x_1)/2$. Fig. 6(a) shows the spatial evolution of λ for identical initial thread size ε_0 with $\varphi = 0.1$, $\chi = 217$, and two different injection capillary numbers Ca_0. As opposed to the fold amplitude A, we find that the wavelength of deformation increases with Ca_0. In the diverging sector (i.e., $x/h \lesssim 4$), the main flow velocity scales as $J \sim x^{-1}$. Since
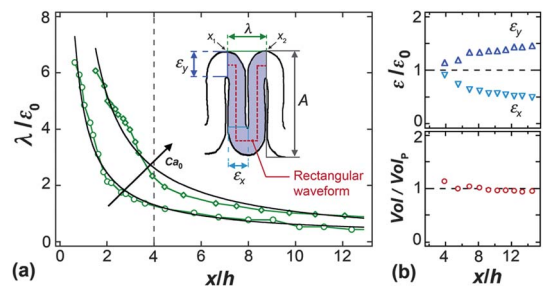
Fig. 6 (a) Normalized wavelength λ/ε_0 versus position x/h for $\varphi = 0.1$, $\chi = 217$, core flow rates Q_1 in µL min^{-1}: 5 ($\bigcirc$), solid line: $\lambda/\varepsilon_0 = 0.165 + 4.6 (x/h)^{-1}$, and 100 ($\diamond$), solid line: $\lambda/\varepsilon_0 = 0.026 + 10.4 (x/h)^{-1}$. Inset: schematic showing geometrical parameters used to characterize folds. (b) Top: evolution of ε_y ($\triangle$) and ε_x ($\triangledown$) along the channel normalized by the initial thread size ε_0 for a case with core flow rates $Q_1 = 50$ µL min^{-1}. Bottom: spatial evolution of normalized fold volume estimated using a rectangular waveform.

threads are convected by the sheath flow, we expect a similar trend for the wavelength evolution, *i.e.*, $\lambda \sim x^{-1}$. Data show relatively good agreement with this scaling argument when wavelengths are fit with the function

$$\lambda/\varepsilon_0 = a + b(x/h)^{-1}, \qquad (2)$$

where a and b are adjustable coefficients [Fig. 6(a)]. Discrepancies between fit and experimental data are observed in part because threads are not initially aligned normal to the flow direction in the diverging channel. Results also show that the wavelength λ continues to decrease in the plane microchannel.

For relatively low viscosity contrasts $\chi \lesssim 217$ and $\lambda/\varepsilon_0 < 2$, the fold evolution is accompanied with a significant stretching of the thread segments aligned normal to the flow direction (*i.e.*, in the y-direction) and a compression of the thread sections arranged with the flow direction (*i.e.*, in the x-direction). To account for this effect, we label the thread diameter placed perpendicular to the main flow field as ε_y, and the thread diameter aligned parallel to the main flow direction as ε_x [Fig. 6(a) – inset]. In Fig. 6(b) (top), we measure the spatial evolution of these quantities normalized by the initial thread diameter, $\varepsilon_x/\varepsilon_0$ and $\varepsilon_y/\varepsilon_0$, and data show a significant departure from unity as the structure is swept away by $L2$ in the microchannel.

The shape of the centerline of compact folds suggests rectangular waveforms. To probe whether the change in the local thread thicknesses ε_x and ε_y is due to the advection of the overall structure by $L2$ in the microchannel or rather caused by the "reflow" of $L1$ within the folded structure, we estimate the volume of a fold using a rectangular waveform approximation: $\mathrm{Vol} \approx \pi[\lambda\varepsilon_y^2/4 + 2(A - \varepsilon_y)\varepsilon_x^2]$, where $A - \varepsilon_y$ is the centerline amplitude. Fig. 6(b) (bottom) shows that the calculated volume normalized with the volume calculated at x_p, $\mathrm{Vol/Vol_P}$, remains approximately constant while the folds evolve in shape. Additional measurements of the volume evolution conducted with the dataset corresponding to $\varphi = 0.1$, $\chi = 217$ and Ca_0 varying between 3 and 60 display similar behavior. This result suggests an elastic-like behavior of the viscous structure for the relatively short convective time-scale associated with the flow of $L2$. This behavior is overall in good accord with the viscous–elastic analogy.[51] It is important to note, however, that although $L1$ may appear "frozen", its fluid behavior is evident through the coalescence of adjacent folds, which can incidentally induce mass transfer across folds, *i.e.*, between different thread sections.

Predicting the shape of capillary folds is a rather intricate task since the evolving fold form depends on many parameters, including the initial thread thickness ε_0, amplitude A, wavelength λ, viscosity contrast χ, injection capillary number Ca_0, and bounding microgeometries. The general trend in the first part of the chamber, however, can be determined by graphing the normalized wavelength λ/ε_0 as a function of the normalized amplitude A/ε_0 for relatively small threads in the viscous regime (*i.e.*, above the critical coalescence capillary number $\mathrm{Ca}_{0,c}$) [Fig. 7]. Data show a monotonic decrease of the spatial period λ with the envelope A and two regimes are identified.

The first regime occurs during the development of the folding instability in the diverging channel and corresponds to cases with long wavelength $\lambda > 2A$. For such weakly deformed threads, we find that the spatial period follows the scaling
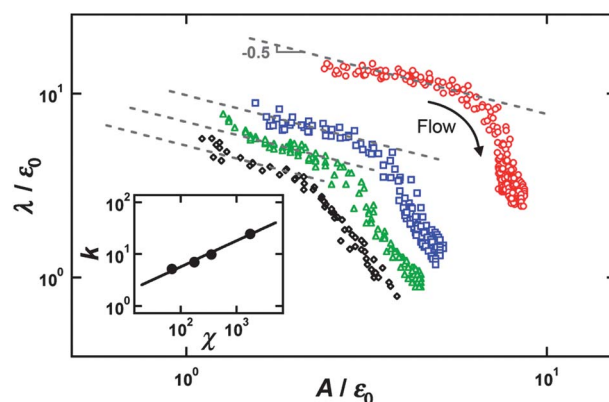
Fig. 7 Initial evolution of normalized fold wavelengths λ/ε_0 as a function of normalized amplitudes A/ε_0 for small threads in the viscous regime, viscosity contrast $\chi = 86$ ($\diamond$), 217 ($\triangle$), 433 ($\square$), and 2172 ($\bigcirc$). Initial thread deformation ($\lambda > 2A$) is shown with dashed lines: $\lambda/\varepsilon_0 = k(A/\varepsilon_0)^{-1/2}$. Inset: evolution of prefactor k with viscosity contrast χ, solid line: $k = 0.57\chi^{1/2}$.

$$\lambda/\varepsilon_0 \approx k(A/\varepsilon_0)^{-1/2}, \qquad (3)$$

with the prefactor k depending on the viscosity ratio $k \approx 0.57\chi^{1/2}$ [Fig. 7 – inset]. In terms of scaling arguments, eqn (3) is consistent with previous finding in the diverging channel (eqn (1) and (2)) where $A \sim x^2$ and $\lambda \sim x^{-1}$.

The second regime corresponds to the behavior of compact structures in the plane channel, *i.e.*, in the short wavelength regime for $\lambda < 2A$. The tendency of the envelope amplitude A to rapidly saturate as the viscosity contrast χ increases combined with the continuous decrease of the wavelength λ in the plane channel precludes the development of simple scaling arguments to characterize this regime.

A general overview of the effect of the viscosity contrast χ on the shape of evolving folds is given in Fig. 8. The partial coalescence regime permits the measurement of the evolution of λ and A over the entire section of the chamber by combining micrographs taken near the inlet and near the outlet of the chamber [Fig. 8(b)]. This technique introduces a small disparity in the envelope amplitude A at the transition between the two regions since different folds are used. Despite the fact that the chamber has a mirror symmetry, experimental data display a significant dissymmetry in the evolution of both A and λ at the inlet and the outlet regions for large viscosity contrasts $\chi = 2172$. In this case, as threads are more solid-like (*i.e.*, more viscous), the feedback effect of the converging flow at the end of the channel is experienced as early as in the middle of the plane channel due to the large momentum transport properties of high-viscosity fluids. For lower viscosity contrasts, however, measurements of both A and λ display a symmetrical behavior, which is overall in good agreement with the flow reversibility property of creeping flows.

From the combined measurements of A and λ, we also calculate the spatial evolution of the amplitude-to-wavelength ratio A/λ over the entire chamber length, L [Fig. 8(c)]. Near the middle of the chamber, this dimensionless parameter reaches a maximum value that can be used to characterize the degree of thread deformations. In particular, experimental findings show that capillary threads having relatively low viscosity contrast ($\chi = 217$) are more corrugated. In addition to the amplitude-
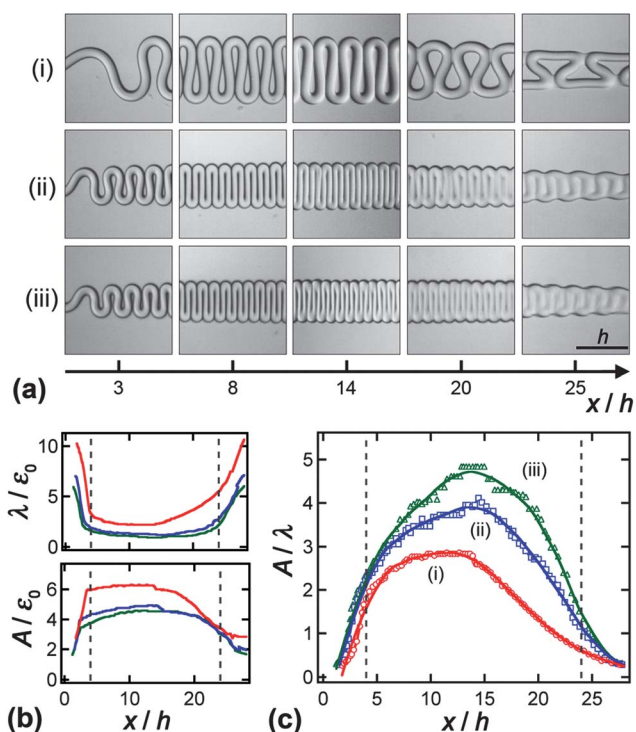
Fig. 8 Thread evolution along the entire chamber for identical flow rates, $Q_1 = 20$ and $Q_2 = 400 \, \mu\text{L min}^{-1}$, and three viscosity ratios: (i) 2172 ($\bigcirc$), (ii) 433 ($\square$), and (iii) $\chi = 217$ ($\triangle$). (a) Chart with micrographs showing fold evolution along the microfluidic chamber. (b) Spatial evolution of normalized wavelength and amplitude in the chamber. (c) Spatial evolution of amplitude-to-wavelength ratio A/λ displaying a maximum value in the chamber central region.

to-wavelength ratio A/λ, the arc-to-wavelength ratio S/λ is another important dimensionless parameter used to describe sinuous shapes of threads as they evolve along the channel.[39]

3.2.3 Velocity and film thickness. In this section, we examine the relationship between envelope amplitude and flow velocity. In particular, non-wetting threads are used to probe the competition between lubrication and wetting phenomena. Fig. 9(a) displays the evolution of the normalized envelope amplitude A/h as a function of the relative velocity V/J_w, where V is the local fold velocity in the plane channel. To produce this curve, we monitor a fold and record its corresponding amplitude and velocity as a function of position using high-speed imaging. Here, we focus on the dataset corresponding to $\varphi = 0.1$ and $\chi = 217$ with an initial capillary number varying between 3 and 30. For low folding amplitudes $A/h < 1.5$, the relative velocity V/J_w is always larger than unity, which corroborates the lubrication assumption since folded structures are convected faster than the multiphase superficial velocity, J_w. Although small discrepancies are observed depending on the injection capillary number Ca_0 in this regime, measurements suggest a scaling such as $A/h \sim (V/J_\text{w})^{-1/2}$. For low capillary numbers ($Ca_0 = 3$), the envelope amplitude grows significantly while the relative velocity decreases below unity with an apparent scaling such as $A/h \sim (V/J_\text{w})^{-1}$ [Fig. 9(a)]. In plane microchannels, parallel streams of miscible fluids display a velocity contrast proportional to their viscosity ratio.[52] In this work, since the viscosity contrast between fluids is
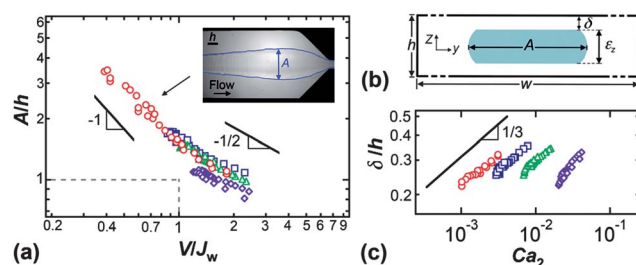
Fig. 9 (a) Evolution of normalized envelope amplitude A/h as a function of relative velocity V/J_w in the plane section for $\varphi = 0.1$, $\chi = 217$, $Ca_0 = 3$ ($\bigcirc$), 6 ($\square$), 15 ($\triangle$), and 30 ($\diamond$). Measurements suggest the scaling $A/h \sim (V/J_\text{w})^{-1/2}$ for small envelope amplitude and $A/h \sim (V/J_\text{w})^{-1}$ for large amplitude. Inset: micrograph of large amplitude for $Ca_0 = 3$. (b) Schematic of the channel cross-section used to estimate film thickness δ. (c) Estimated normalized film thickness $\delta/h = [1 - Q_1/(VAh)]/2$ as a function of sheath fluid capillary number Ca_2 based on pile velocity: $Ca_2 = \eta_2 V/\gamma_{12}$ for data displayed in (a), solid line $\delta/h \sim Ca_2^{1/3}$.

very large ($\chi = 217$) while the relative velocity is close to unity, we conclude that, even for large amplitudes, capillary structures remained lubricated by a thin film of $L2$ due to the non-wetting property of our capillary threads.

Fig. 9(b) displays a schematic of the channel cross-section in the y–z plane for a plain structure with amplitude A and thickness ε_z. Using a mass conservation argument and direct measurements of the amplitude A and velocity V from high-speed images, we estimate the evolution of the film thickness δ of $L2$ at the walls assuming $Q_1 = VA\varepsilon_z$ and $\varepsilon_z = h - 2\delta$. Fig. 9(c) shows the evolution of the normalized film thickness $\delta/h = [1 - Q_1/(VAh)]/2$ as a function of the continuous phase capillary number $Ca_2 = \eta_2 V/\gamma_{12}$ with the scaling $\delta/h \sim Ca_2^{1/3}$. Although this approximation shows a consistent trend, it also overestimates the actual thickness since our capillary structures are punctured when they are not fully coalesced.

3.3 Capillary microstructures

The combination of viscous folding phenomena and interfacial tension effects leads to the formation of peculiar capillary structures in the microfluidic platform. The ability to control the initial shape and the residence time of threads with flow rates of injection enables the examination of thread aging processes and various emulsification mechanisms are identified.

3.3.1 High-viscosity fluid emulsification: breakup by folding. Here, we inspect the breakup regime that occurs for small thread sizes and large capillary numbers [Fig. 2(a)]. We show in particular that depending on flow conditions, the system can take different routes to minimize fluid interfacial area, such as coalescence or breakup. Fig. 10 displays micrographs of capillary threads in the chamber for a range of flow rate ratios. As the folding amplitude A increases with the initial thread size ε_0, the most efficient mechanism for reducing the interfacial area of large threads is fold coalescence [Fig. 10 – $\varphi = 1/15$]. When the initial thread size ε_0 is sufficiently small and the resulting folding amplitude A in the central region is less than the cell gap, $A \lesssim h$, folded structures can also evolve in the z-direction. In this situation, as folds become more compacted along the flow direction,
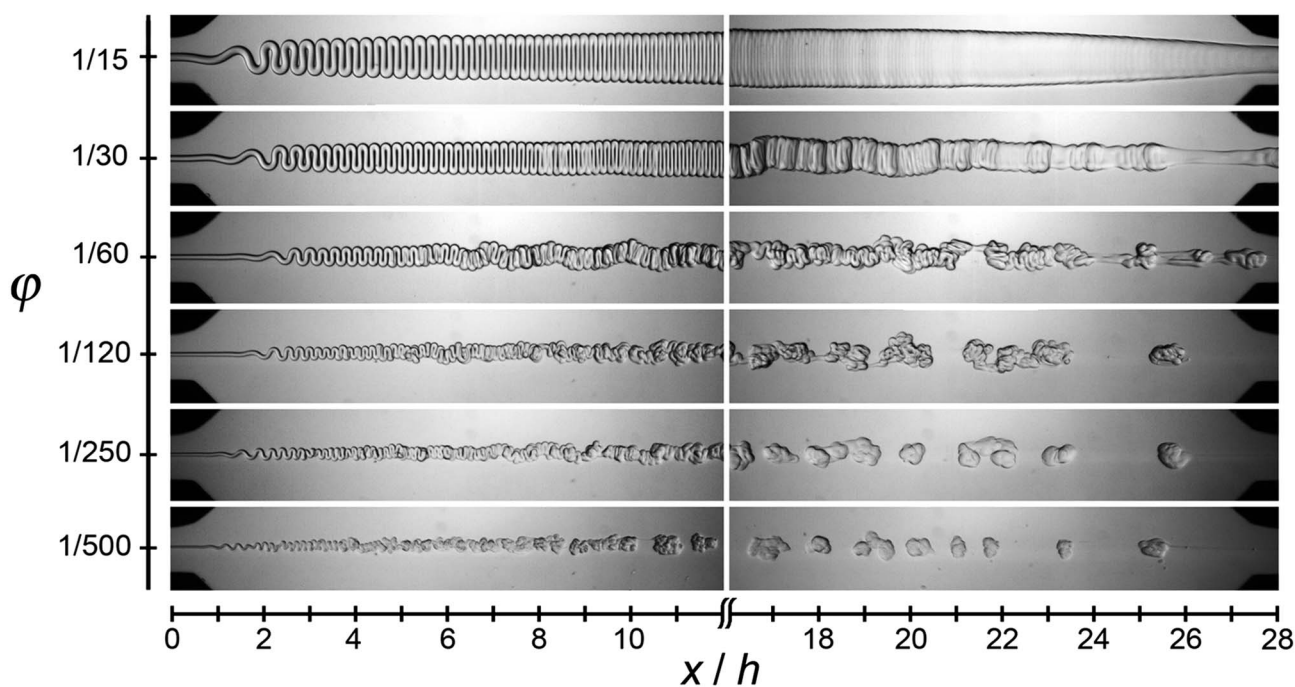
Fig. 10 Breakup of capillary threads by viscous folding. Flow rate ratio $\varphi = Q_1/Q_2$, viscosity contrast $\chi = 217$, flow rates in µL min^{-1}: $\varphi = 1/15$, complete coalescence regime ($Q_1 = 10$ and $Q_2 = 150$); $\varphi = 1/30$, coalescence between folds ($x/h \sim 8$) induce secondary folding ($Q_1 = 10$ and $Q_2 = 300$); $\varphi = 1/60$, onset of breakup ($Q_1 = 10$, $Q_2 = 600$); $\varphi = 1/120$, fully detached heterogeneous structures ($Q_1 = 5$ and $Q_2 = 600$); $\varphi = 1/250$, smooth capillary structures ($Q_1 = 1$ and $Q_2 = 250$); $\varphi = 1/500$, breakup near diverging channel ($Q_1 = 1$ and $Q_2 = 500$).

adjacent folds can slide on top of one another and coalesce [Fig. 10 – $\varphi = 1/30$, $x/h \sim 8$]. This reduced degree of confinement permits distorted viscous filaments to evolve in the y–z plane and produces secondary folding phenomena (*i.e.*, large-scale undulations of already folded threads). Small disturbances in the z-direction are further amplified given the thin-gap parallel plate geometry of the chamber with a typical parabolic velocity profile of $L2$ in the z-direction. Overall, irregular thread structures are subject to the Rayleigh–Plateau instability with fluid accumulation into crests [Fig. 10 – $\varphi = 1/30$, $x/h \sim 24$]. As the thread size further decreases, fold coalescence and secondary folding occur upstream in the chamber. The additional degree of freedom for small threads to deform in the z-direction introduces significant secondary folding and finite broken lumps of $L1$ having different degrees of coalescence are observed [Fig. 10 – $\varphi = 1/60$ and $1/120$]. Finally, for very small threads, the viscous blobs appear smoother when they reach the end of the chamber [Fig. 10 – $\varphi = 1/250$ and $1/500$]. This phenomenon illustrates the complex interplay between viscous and capillary instabilities in confined microsystems. Here, the mechanisms observed suggest that the "breakup by folding" phenomenon permits the continuous emulsification of high-viscosity fluids in microgeometries at fast flow rates and low volumetric fractions.

3.3.2 Low-viscosity fluid emulsification: droplet-decorated streams. We previously discussed the possibility to use thin threads to disperse small quantities of a high-viscosity fluid into a low-viscosity phase. In this last section, we show that thick threads can be utilized to emulsify minute amounts of a low-viscosity fluid into a highly viscous phase through the entrapment of the sheath fluid $L2$ into the folded structure made of $L1$. For

unbounded systems, viscous jets impinging on the free surface of the same liquid in air can entrain air bubbles into the pool[53,54] and form complex bubble patterns, including spiral waves.[55]

Here, the combination of viscous folding and capillary instabilities with self-lubrication phenomena in constrained microgeometries can lead to the "reverse" emulsification of the sheath fluid into the pile of the more viscous liquid. Over the range of parameters investigated, we find that this dynamical process strongly depends on the viscosity contrast χ, which sets the overall fold style (such as flat or curly bends). In particular, the regime of droplet inclusion into the pile is only observed when
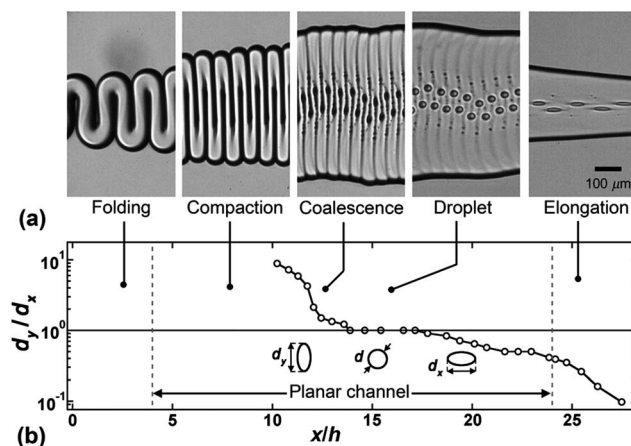
Fig. 11 Formation of droplet-decorated streams. (a) Flow history of a folding thread along the chamber, fluid pair $G2$, $Q_1 = 60$ and $Q_2 = 300$ µL min^{-1}. (b) Evolution of the droplet aspect ratio d_y/d_x as a function of location x/h in the microchamber.

the viscosity of the silicone oil $L1$ is $\nu_1 = 500$ cSt. Therefore, to gain more insights into this emerging phenomenon, we conduct additional experiments where the viscosity of the silicone oil $L1$ is fixed at $\nu_1 = 500$ cSt and $L2$ consists of mixtures of isopropanol and ethanol. We examine three fluid pairs labeled with $G1$ ($L2$ is made of pure isopropanol, $\chi = 217$), $G2$ ($L2$ is made of 50% isopropanol and 50% ethanol in volume, $\chi = 309$), and $G3$ ($L2$ is made of 20% isopropanol and 80% ethanol, $\chi = 374$). Overall, these three fluid pairs display similar interfacial tension γ_{12} ranging between 1.1 and 2.5 mN m^{-1}.

Fig. 11 illustrates the spatial evolution of a capillary structure that leads to the formation of a "droplet-decorated stream" along the microfluidic chamber for the fluid pair $G2$. Different stages of droplet formation are identified. First, the thread folds in the diverging channel and the folding amplitude A increases in the first part of the planar section. The growth of the envelope amplitude A is accompanied by the thread compaction (i.e., diminution of the wavelength λ) and a reduction of the film thickness δ along the flow direction. For our specific range of viscosity contrasts, the coalescence of neighboring folds occurs both at the center and at the edge of the pile, thereby entrapping small quantity of the low-viscosity fluid $L2$ between folds. For small film thicknesses $\delta/h \ll 1$, the small amount of $L2$ cannot escape from the pile and remains embedded in high-viscosity liquid $L1$ in the form of droplets.

The droplet morphological changes are characterized by the evolution of their aspect ratio d_y/d_x, where d_y is the droplet length in the direction normal to the flow (i.e., in the y-direction) and d_x is the droplet length in the direction parallel to the main flow (i.e., in the x-direction) [Fig. 11(b)]. During the process of liquid

entrapment due to fold coalescence, which typically occurs in the middle of the planar section, droplets initially have a large aspect ratio $d_y/d_x > 1$ as they form. A droplet aspect ratio on the order of unity $d_y/d_x \approx 1$ is used to characterize the main droplet size $d = d_y = d_x$. Near the converging section, embedded droplets are observed to elongate along the flow direction with $d_y/d_x < 1$. The droplet elongation phenomenon in extensional flows has also been observed in diverging and converging microchannels as well as in four-roll mill apparatuses.[22,56]

The 3D droplet formation mechanism can be visualized with a time-series of a coalescing thread [Fig. 12(a)]. In this case study, folds start to coalesce from the center of the structure while displacing $L2$, which accumulates into a cylinder-like shape with vertical diameter $d_z \approx h - 2\delta$ as indicated with the circle on Fig. 12(a)-(i). The fold fusion from the edge of the pile imprisons $L2$ in the fold, primarily in the y-direction [Fig. 12(a)-(ii)]. At this point, the structure appears similar to the ones observed for larger viscosity contrast with "holes" between partially coalesced folds, e.g., Fig. 2(b). At a later stage, the change in the droplet appearance suggests that fold coalescence also occurs in the z-direction, which breaks up the $L2$ cylinder into two droplets located on each side of the pile near the top and bottom walls [Fig. 12(a)-(iv)]. This statement is substantiated by the fact that folding lines can be seen across the droplets and droplets appear to become mostly spherical in shape.

When the droplet aspect ratio is equal to unity, we measure the average droplet size d in the pile as a function of the flow rate ratio φ [Fig. 12(b)]. Experimental findings show that the normalized droplet size scales with

$$d/h \approx a\varphi^{1/2}, \qquad (4)$$

with the constant $a = 0.3$. The typical droplet size is about an order of magnitude smaller than the chamber gap h and is overall proportional to the fold amplitude A. As the amplitude A increases, we also observe a succession of smaller droplets along each coalescence line [Fig. 12(c)]. We label primary droplets as $D1$ and secondary droplets as $D2$. This droplet formation mechanism leads to intricate morphologies. In this series of experiments, we noticed that for small flow rate ratios $\varphi < 0.1$, the droplets form between the pile centerline and the pile edge. As φ rises, droplets form near the centerline and beyond the centerline for even larger φ [Fig. 12(c) – top].

4. Conclusion

In this article, we discuss the evolution of capillary structures made of high-viscosity fluids in a long microfluidic chamber. The viscous folding instability is used to deform non-wetting threads that are ensheathed within immiscible fluids into complex structures with large interfacial areas. Adjusting the residence time of these structures in the chamber with the flow rates of injection allows us to produce various degrees of fold coalescence.

We first develop a phase-diagram where three distinct regimes (breakup, partial coalescence, and full coalescence) are located as a function of the injection capillary number Ca_0 and the initial dimensionless thread size ε_0/h for a viscosity contrast χ ranging between 86 and 2172. Analysis of the spatial evolution of the
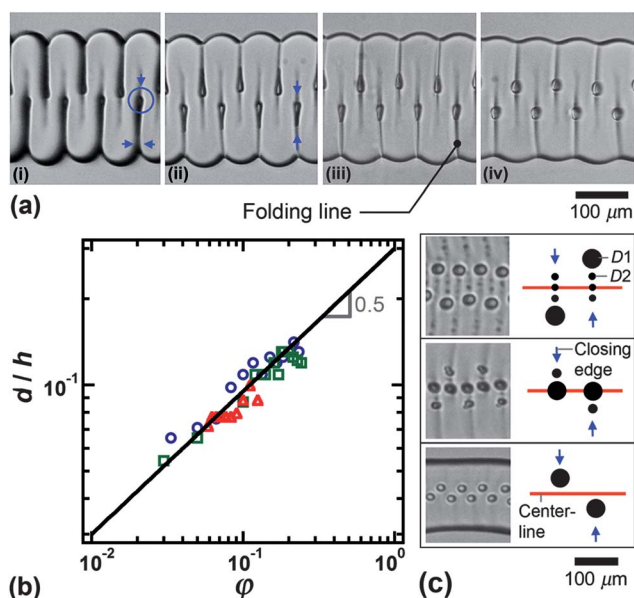
Fig. 12 Morphology of droplet-decorated streams. (a) From left to right: time-series ($\Delta t = 2$ ms) of droplet-forming pile, arrows indicate the coalescence direction, fluid pair $G3$, $Q_1 = 50$ and $Q_2 = 500$ µL min^{-1}. (b) Average droplet size d/h as a function of flow rate ratio φ, symbols for fluid pairs: $G1$ ($\triangle$), $G2$ ($\bigcirc$), and $G3$ ($\square$). Solid line: $d/h = 0.3\varphi^{1/2}$. (c) Location of primary droplets $D1$ with respect to pile centerline. Fluid pair $G2$, flow rates in µL min^{-1}, fixed $Q_2 = 300$, from top to bottom: $Q_1 = 70$, 50, and 10.

envelope amplitude of bended structures reveals that fold development is more prominent at low capillary numbers. We interpret this result based on the reduced flow lubrication properties (*i.e.*, small film thickness δ) associated with low Ca_0. Next, we show that in the partial coalescence regime, structures reach their maximum amplitude A in the middle of the chamber. The developed scaling laws in this case are in good agreement with previous work conducted with miscible fluid threads in similar environments. The spatial period of fold λ is found to continuously decrease along the flow direction. In particular, we demonstrate that the thread size evolves for ultracompact structures. In the diverging section, experimental findings suggest that in the long wavelength regime $\lambda > 2A$, the spatial period and amplitude of thread scale as $\lambda/\varepsilon_0 \approx a\chi^{1/2}(A/\varepsilon_0)^{-1/2}$, with $a = 0.57$. The sinuous shape parameter A/λ reaches a maximum in the chamber center. We correlate the measured fold velocity V with the average multiphase flow velocity J_W and show that although structures are lubricated, their velocity decreases when the amplitude A is larger than the parallel plate gap thickness h.

The manipulation of highly viscous oils with low surface tension liquids in microchannel leads to a variety of relatively unexplored emulsification mechanisms. In particular, we examine the influence of secondary folding phenomena on the production of high-viscosity droplets at high-capillary numbers. For relatively low viscosity contrasts χ ranging between 218 and 374, we investigate the formation of droplet-decorated streams, which are characterized by the inclusion of low-viscosity droplets into the pile of the high-viscosity fluid through a complex fold coalescence phenomenon. As droplets are swept away at the envelope velocity, they experience a large change in their aspect ratio. This emergent phenomenon can produce regular assemblies of multi-scale droplets, the size of which can be orders of magnitudes smaller than the confinement length-scale h. The formation of these droplets also results from the local variations in the film thickness δ caused by the folding instability. These variations induce film rearrangements that give rise to a local capillary pressure gradient in the film and drains $L2$ toward the wedge formed by each coalescence line. This mechanism is somehow reminiscent of dry foam behavior where liquid is collected into plateau borders and vertex due to interfacial curvature.[57,58] The interplay between the non-wetting dynamic properties of threads and the formation of embedded droplets near the top and bottom walls of plane microchannels requires further work.

In conclusion, this study provides a new understanding of the influence of coalescence on viscous buckling phenomena using continuous microflow systems. The ability to produce morphologies having different degrees of coalescence is promising for the elaboration of slender microstructures with photosensitive materials treatable with UV light.[59] In addition, precise interfacial control of viscous substances with low viscosity fluids in miniature platforms should facilitate the transport of complex fluids with reactive solvents for intervening on soft matter. Overall, this work demonstrates the possibility to create a range of emerging fluid phenomena by combining viscous and capillarity instabilities. These novel flow destabilization processes can be used to devise original methods for tailoring the properties of soft materials using artificial microgeometries.

References

1 G. Homsy, *Annu. Rev. Fluid Mech.*, 1987, **19**, 271–311.
2 P. Sun, B. Wang, J. Yao, L. Zhang and N. Xu, *Ind. Eng. Chem. Res.*, 2010, **49**, 1259.
3 B. Gopalan and J. Katz, *Phys. Rev. Lett.*, 2010, **104**, 054501.
4 A. Aiyejina, D. P. Chakrabarti, A. Pilgrim and M. K. S. Sastry, *Int. J. Multiphase Flow*, 2011, **37**, 671.
5 B. Chan, N. J. Balmforth and A. E. Hosoi, *Phys. Fluids*, 2005, **17**, 113101.
6 K. Miyake, T. Tanaka and P. L. McNeil, *PLoS Biol.*, 2006, **4**, 1525.
7 C. A. Vasconcellos, P. G. Allen, M. E. Wohl, J. M. Drazen, P. A. Janmey and T. P. Stossel, *Science*, 1994, **263**, 969.
8 D. D. Joseph, K. Nguyen and G. S. Beavers, *J. Fluid Mech.*, 1984, **141**, 319–345.
9 C. R. Carrigan and J. C. Eichelberger, *Nature*, 1990, **343**, 248.
10 D. D. Joseph and Y. Y. Renardy, *Fundamentals of Two-Fluid Dynamics. Part II: Lubricated Transport, Drops and Miscible Liquids*, Springer-Verlag, New York, 1993.
11 J. Wang and D. F. James, *J. Rheol.*, 2011, **55**, 1103.
12 T. M. Squires and S. R. Quake, *Rev. Mod. Phys.*, 2005, **77**, 977–1026.
13 P. Garstecki, M. Fuerstman, H. A. Stone and G. W. Whitesides, *Lab Chip*, 2006, **6**, 437–446.
14 C. N. Baroud, F. Gallaire and R. Dangla, *Lab Chip*, 2010, **10**, 2032.
15 V. van Steijn, C. R. Kleijn and M. T. Kreutzer, *Phys. Rev. Lett.*, 2009, **103**, 214501.
16 L. Frenz, K. Blank, E. Brouzes and A. D. Griffiths, *Lab Chip*, 2009, **9**, 1344.
17 T. Cubaud, M. Sauzade and R. Sun, *Biomicrofluidics*, 2012, **6**, 022002.
18 W. Jeong, J. Kim, S. Kim, L. Sanghoon, G. Mensing and D. J. Beebe, *Lab Chip*, 2004, **4**, 576.
19 T. Cubaud and T. G. Mason, *Phys. Rev. Lett.*, 2006, **96**, 114501.
20 T. Cubaud and T. G. Mason, *New J. Phys.*, 2009, **11**, 075029.
21 J. Eggers, *Rev. Mod. Phys.*, 1997, **69**, 865.
22 H. A. Stone, *Annu. Rev. Fluid Mech.*, 1994, **26**, 65–102.
23 J. Eggers and E. Villermaux, *Rep. Prog. Phys.*, 2008, **71**, 036601.
24 L. G. Leal, *Phys. Fluids*, 2004, **16**, 1833–1851.
25 H. Yang, C. C. Park, Y. T. Hu and L. G. Leal, *Phys. Fluids*, 2001, **13**, 1087–1106.
26 S. W. Morris, J. H. P. Dawes, N. M. Ribe and J. R. Lister, *Phys. Rev. E: Stat., Nonlinear, Soft Matter Phys.*, 2008, **77**, 066218.
27 J. D. Buckmaster, *J. Fluid Mech.*, 1973, **61**, 449–463.
28 M. Maleki, M. Habibi, R. Golestanian, N. M. Ribe and D. Bonn, *Phys. Rev. Lett.*, 2004, **93**, 214502.
29 N. M. Ribe, *Proc. R. Soc. London, Ser. A*, 2004, **460**, 3223.
30 N. M. Ribe, J. R. Lister and S. Chiu-Webster, *Phys. Fluids*, 2006, **18**, 124105.
31 N. M. Ribe, M. Habibi and D. Bonn, *Annu. Rev. Fluid Mech.*, 2012, **44**, 249.
32 P. G. Saffman and G. Taylor, *Proc. R. Soc. London, Ser. A*, 1958, **245**, 312.
33 J. S. Langer, *Science*, 1989, **243**, 1150–1156.
34 P. G. de Gennes, *Rev. Mod. Phys.*, 1985, **57**, 827–863.
35 T. D. Blake, *J. Colloid Interface Sci.*, 2006, **299**, 1–13.
36 D. Quéré, *Annu. Rev. Mater. Res.*, 2008, **38**, 71.
37 S. Herminghaus, M. Brinkmann and R. Seemann, *Annu. Rev. Fluid Mech.*, 2008, **38**, 101.
38 C. Cottin, H. Bodiguel and A. Colin, *Phys. Rev. E: Stat., Nonlinear, Soft Matter Phys.*, 2011, **84**, 026311.
39 T. Cubaud, B. M. Jose and S. Darvishi, *Phys. Fluids*, 2011, **23**, 042002.
40 M. J. Madou, *Fundamentals of Microfabrication: The Science of Miniaturization*, CRC, 2002.
41 E. H. Klaassen, K. Petersen, J. M. Noworolski, J. Logan, N. I. Maluf, J. Brown, C. Storment, W. McCulley and G. T. A. Kovacs, *Sens. Actuators, A*, 1996, **52**, 132–139.
42 S. Darvishi and T. Cubaud, *J. Fluids Eng.*, 2011, **133**, 031203.
43 T. Cubaud and T. G. Mason, *Phys. Fluids*, 2008, **20**, 053302.

44 N. Rashidnia, R. Balasubramaniam and D. Del Signore, *AIChE J.*, 1992, **38**, 615–618.

45 M. Wu, T. Cubaud and C.-M. Ho, *Phys. Fluids*, 2004, **16**, L51.

46 F. P. Bretherton, *J. Fluid Mech.*, 1961, **10**, 166.

47 M. T. Kreutzer, F. Kapteijn, J. A. Moulijn and J. J. Heiszwolf, *Chem. Eng. Sci.*, 2005, **60**, 5895–5916.

48 J. Ratulowski and H.-C. Chang, *Phys. Fluids A*, 1989, **1**, 1642.

49 N. M. Ribe, *Phys. Rev. E: Stat. Phys., Plasmas, Fluids, Relat. Interdiscip. Top.*, 2003, **68**, 036305.

50 M. Skorobogatiy and L. Mahadevan, *Europhys. Lett.*, 2000, **52**, 532.

51 L. D. Landau and E. M. Lifshitz, *Theory of Elasticity*, Pergamon Press, Oxford, 1986.

52 T. Cubaud and T. G. Mason, *Phys. Rev. E: Stat., Nonlinear, Soft Matter Phys.*, 2008, **78**, 056308.

53 E. Lorenceau, D. Quéré and J. Eggers, *Phys. Rev. Lett.*, 2004, **93**, 254501.

54 B. Pouligny and M. Chassande-Mottin, *Phys. Rev. Lett.*, 2008, **100**, 154501.

55 M. Habibi, P. C. F. Moller, N. M. Ribe and D. Bonn, *Europhys. Lett.*, 2008, **81**, 38004.

56 J. T. Cabral and S. D. Hudson, *Lab Chip*, 2006, **6**, 427–436.

57 R. G. Larson, *The Structure and Rheology of Complex Fluids*, Oxford University Press, Inc., New York, 1999.

58 S. A. Koehler, H. A. Stone, M. P. Brenner and J. Eggers, *Phys. Rev. E: Stat. Phys., Plasmas, Fluids, Relat. Interdiscip. Top.*, 1998, **58**, 2097.

59 D. Dendukuri, D. C. Pregibon, J. Collins, T. A. Hatton and P. S. Doyle, *Nat. Mater.*, 2006, **5**, 365–369.